

FOCUS STACKING PHOTOGRAMMETRY FOR MICRO- SCALE ROUGHNESS RECONSTRUCTION: A METHODOLOGICAL STUDY

MARCIN OLKOWICZ^{a*} (molk@pgi.gov.pl)

MARCIN DABROWSKI^{ab} (mdabr@pgi.gov.pl)

ANNE PLUYMAKERS^{b§} (Anne.Pluymakers@tudelft.nl)

^a*Computational Geology Laboratory, Polish Geological Institute – National Research
Institute, Wrocław, Poland*

^b*Physics of Geological Processes, The Njord Center, University of Oslo, Norway*

*Corresponding author

§Now at TU Delft, Delft, The Netherlands

Abstract

In close-range applications, it is unclear whether optical photogrammetry is capable of accurately reconstructing submillimetre-scale roughness. This paper presents a study of fine-scale rock fracture roughness measurements with a careful assessment of the error. The workflow combines the techniques of structure from motion with focus stacking, using consumer-grade equipment and free or affordable software. The approach is tested firstly with synthetic data to check the influence of the number and position of cameras, object texture and image processing using focus stacking. Secondly, the optimised workflow is used to measure a natural shale rock fracture surface. To estimate the accuracy, the results were compared with a high-precision reference dataset provided by white-light interferometry. The standard deviation of error in the method is 6.5 μm , and is related with morphological structures with wavelengths below 150 μm and amplitudes smaller than 10 μm .

KEYWORDS: accuracy, close range photogrammetry, focus stacking, roughness, structure from motion, shale rock fracture

INTRODUCTION

IN GEOLOGICAL, GEOMECHANICAL AND GEOENGINEERING STUDIES, rock fracture morphology is a subject of interest since a wide variety of structures develop on fracture surfaces, reflecting the fracture dynamics. Tectonic structures such as rib and ripple marks, hackle fringes or plumose structures in general, together with slickenside lineation (Bahat, 1991; Twiss and Moores, 2007), often provide useful information about fracture origin, fracture wall displacement history and far field stress directions (Angelier, 1984; Aleksandrowski, 1985;

Bahat, 1987; Degraff and Aydin, 1987; Petit, 1987). An example is where roughness scaling is used to determine whether microfractures in a shale rock core originated at a depth of several kilometres or at the surface after core recovery (Pluymakers et al., 2017). Fracture surface structures may be also used for inferring fault and earthquake dynamics (Brodsky et al., 2011; Candela et al., 2012). In geomechanical and geoenvironmental studies, roughness measurements are used to investigate fracture shear strength through the joint roughness coefficient (JRC) (Barton, 1973; Barton and Choubey, 1977; Li and Huang, 2015; Ficker, 2017; Zhang et al., 2017). Since, with increasing confining pressure and thus burial depth, fractures close, the mismatch of roughness on opposing fracture walls is a way to estimate the resulting aperture distribution (Tsang and Witherspoon, 1981; Walsh, 1981; Cook, 1992; Lanaro, 2000). The distribution of local aperture plays an important role in fluid flow and transport in fractured media, controlling the degree of flow channelling and the effective transmissivity (Zimmerman and Bodvarsson, 1996; Mourzenko et al., 2001; Brush and Thomson, 2003; Schmittbuhl et al., 2008; Babadagli et al., 2015; Wang et al., 2015).

Fracture roughness can be viewed as any deviation from the overall fracture plane. The morphology of engineered surfaces can often be separated into two clear components: a long-wavelength regular waviness and a small-scale noisy roughness (Raja et al., 2002). While geological surface structures, such as rib marks, may be characterised by distinct length scales, multiple studies have demonstrated the general self-affine character of natural wall roughness of well-developed faults in geological materials (Poon et al., 1992; Xie et al., 1999; Candela et al., 2012). Thus, fractal measures such as the Hurst exponent or the fractal dimension (often obtained from a Fourier power spectrum versus a wavelength or wavenumber plot – see, for example, Candela et al. (2012)) and the root mean square (RMS) roughness at a reference length scale, are required to give an appropriate description of such scale-independent structures (Mandelbrot, 1983; Gallant et al., 1994; Odling, 1994; Brown, 1995). However, other useful descriptors, such as roughness kurtosis or skewness, and the mean spacing of adjacent peaks (Gadelmawla et al., 2002), are also used to quantify natural surface roughness (Zou et al., 2015).

In earth sciences, morphological features of widely varying length scales are examined depending on the application (Fujii et al., 2007; Candela et al., 2012; Ameli et al., 2013; Thom et al., 2017); accurate measurements are the key input data for the following statistical analysis. For studies focused on small-scale roughness, both the sampling resolution and measurement accuracy are crucial factors in obtaining high-quality datasets (Yong et al., 2018). A wide spectrum of measurement techniques, targeting different observation lengths, has been developed over the last 50 years. This includes: (1) contact methods such as the Barton comb (Morelli, 2014) and the stylus profilometer (Poon and Bhushan, 1995); (2) atomic force microscopy (Thom et al., 2017); and (3) non-invasive optical techniques such as confocal microscopy (Ficker and Martišek, 2012), white-light interferometry (Renard et al., 2012), laser triangulation (Martínez et al., 2010), structured light projection (Tatone and Grasselli, 2012) and photogrammetry (Lee and Ahn, 2004). The lateral and vertical resolution and accuracy of the measurement techniques depend on the underlying physical principles; each technique therefore has its own restrictive application range. Moreover, the cost of equipment varies greatly; however, consumer-grade cameras and thus photogrammetry-based methods may represent one of the most cost-effective options.

Photogrammetry is an optical technique of reconstructing the three-dimensional (3D) geometry of measured objects based on images taken from different angles and camera positions. Wickens and Barton (1971) proposed that photogrammetry could be used as a method of roughness measurements for rock fractures. With the advance of digital cameras, photogrammetry has been successfully applied in both laboratory assessments (Lee and Ahn, 2004; Fujii et al., 2007; Nilsson et al., 2012) and field measurements (Fujii et al., 2007;

Haneberg, 2007; Bistacchi et al., 2011; Corradetti et al., 2017a) of fault and fracture wall roughness at different length scales. It has also been recently applied to surface tracking in analogue experiments (Heng et al., 2010; Galland et al., 2016), fold analysis (Vollgger and Cruden, 2016; Corradetti et al., 2017b), fault or fracture spatial analysis (Lato and Vöge, 2012; Vollgger and Cruden, 2016), stratigraphy (Nieminski and Graham, 2017) and palaeontology (Lockley et al., 2016). Nowadays, thanks to the intensive development of computer technology and digital photography, photogrammetry has become an affordable and popular method of 3D imaging. However, even though photogrammetry has been extensively applied to measuring natural surface roughness, this technique is typically used without performing rigorous estimates of the measurement accuracy. In fact, it is unclear whether optical photogrammetry is a viable technique for reconstructing submillimetre-scale roughness for surface areas on the order of a few square centimetres.

The spatial resolution of photogrammetric reconstruction depends primarily on the ground sample distance (GSD), which is defined as the area covered by a single pixel depending on the magnification and camera resolution. The reconstruction accuracy depends on a sufficient overlap of input images and their positions (Wenzel et al., 2013). Image quality, which is ultimately controlled by the camera's CCD/CMOS sensor and lens properties, also plays an important role. Image sharpness is the most important quality parameter; it can be affected by undesired camera movements during exposure, inappropriate lighting conditions or diffraction effects with a small relative aperture (high f-number). The textural features of the sample may affect the reconstruction accuracy due to their influence on the detection and matching of the keypoints and thereby recovering camera positions. In principle, sharp imaging can only be achieved within a certain depth range (the depth of field (DOF)) for a given distance between the camera and the object (Savazzi, 2011). Therefore, measuring surface roughness in fine-grained rocks by photogrammetry is restricted by the limitations of the plane of maximum focus.

This study combines standard photogrammetry with focus stacking (FS) to develop a low-cost system for measuring fine-scale roughness. (*Focus stacking* combines multiple images, taken at different focus distances, to produce a resultant image with a greater DOF than any of the source images individually.) An estimate of the accuracy of such photogrammetric reconstructions of low-amplitude (tens to hundreds of micrometres) fracture roughness in shales is also made. Synthetic tests were performed to assess the errors inherent to the reconstruction algorithm, depending on the input coverage and textural features of the surface. The level of distortions associated with the FS procedure is also quantified, together with their impact on the final accuracy. Finally, the recommendations developed are used to produce a photogrammetric reconstruction of the fracture roughness in a shale sample; the results are compared to the corresponding high-resolution white-light interferometry images.

METHODS

Photogrammetry Software

VisualSFM is a free and open-source graphical user interface (GUI) application for photogrammetric 3D reconstruction. Its components include SiftGPU (scale-invariant feature transform (SIFT) for a graphics processing unit (GPU)), multicore bundle adjustment (MBA), Patch-based Multi-View Stereo 2 (PMVS2) and Clustering Views for Multi-View Stereo (CMVS) (Wu, 2013). This software suite enables a fully automatic structure-from-motion (SfM) reconstruction, starting from a set of images taken from various positions and

angles, and ending with a dense 3D point cloud. The workflow is summarised in the following four steps:

- (1) Keypoints that exhibit a strong local contrast are detected by a standard difference of Gaussians (DoG) method and matched between input images using the SiftGPU routine (Wu, 2007). The resulting list contains keypoints detected on at least two images.
- (2) The MBA procedure (Wu et al., 2011) is executed to calculate the camera position and orientation (exterior orientation (extrinsic parameters)), restore the camera's interior orientation (intrinsic camera parameters) and finally create a sparse point-cloud reconstruction based on the keypoints.
- (3) The PMVS2/CMVS software (Furukawa and Ponce, 2010) is used to reconstruct a dense texturised point cloud based on the previously determined camera positions (the output from the MBA). The software supports multicore computations, which reduces the overall reconstruction time. To control the reconstruction process, the user has direct access to multiple, explicit reconstruction parameters.
- (4) The components in (1), (2) and (3) are wrapped within VisualSFM, which provides a user-friendly graphic interface to control the reconstruction. According to software benchmarks (Schöning and Heidemann, 2015; Terpstra et al., 2016; Bianconi et al., 2017), the VisualSFM workflow provides high-quality results in terms of their accuracy and precision, but, in general, the performance of SfM software can be highly case-dependent.

For the reconstructions in this research, the default software settings were used except for a change in the soft limit for detected features to 100 000 and in the maximum working dimension in SiftGPU to 8000. The software was run on a laptop equipped with a quad-core i7 4720HQ 2.6/3.6 GHz CPU, GeForce GTX 960M 4 GB GPU and 16 GB RAM.

Image Acquisition Hardware

Both dedicated hardware solutions and tailored procedures were used to collect high-quality input images. Images were captured with a full-frame Canon 5DS R 50.3 megapixel (8868×5792) camera with a sensor size of $36 \text{ mm} \times 24 \text{ mm}$. The 5DS R type offers a low-pass filter cancellation effect, which results in greater sharpness and finer detail of acquired images (Canon, 2017). To obtain high-quality images, a low distortion Canon EF 100 mm f/2.8L IS USM macro lens was used. This lens allows for a maximal magnification of 1:1. A 30 cm distance between the camera sensor and the object results in a field of view equivalent to the image sensor size ($36 \text{ mm} \times 24 \text{ mm}$), which corresponds to the same pixel pitch (the pixel size on the camera sensor) and GSD ("pixel size in object space units" (Granshaw, 2016)), namely $4.14 \mu\text{m}$. The camera was mounted on a Cognisys macro rail system for easy camera distance adjustment (Fig. 1). The lighting was provided by three fixed fluorescent lamps, with a colour temperature of 6500 K and a colour rendering index of over 90. The lamps were placed 1 to 2 m away on the stabilised tripods. Two of them were placed on either side of the sample, with the third one placed centrally above the sample. The lighting system provides an almost shadowless environment and an even illumination of the entire sample surface. To suppress ambient vibrations and reduce undesired camera and sample movements, the experimental equipment was mounted on a 250 kg table. The sample remained stationary during acquisition while the measuring system (camera, macro rail and tripod head) was attached to the holder, which can be

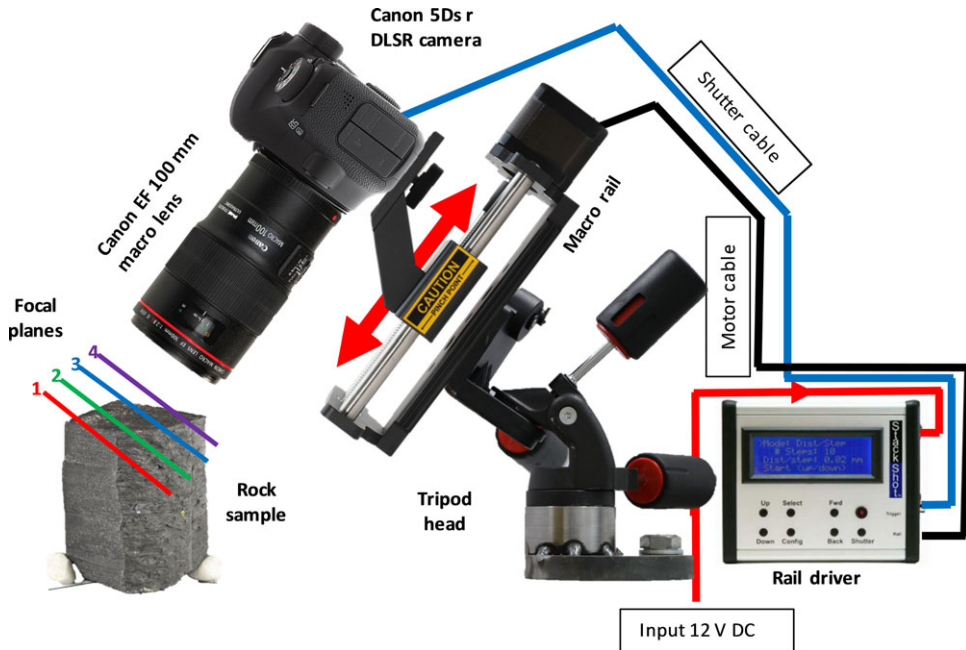


FIG. 1. Image acquisition hardware. During stepwise back movement of the camera (attached to a macro rail), the camera focus distance remains constant and single shots are taken with the focus on consecutive focal planes (shown here with different colours and numbers). The entire process is automated and controlled by the rail driver. Subsequently, focus stacking is used to create a single, complete sharp image (extended DOF image) of the surface. To obtain a set of DOF images captured from different orientations, the image measuring system is moved with respect to the stationary sample.

screwed to the table in any desired orientation. To change the camera viewpoint, the holder was moved to the next position.

Focus Stacking Technique

The consequence of using a high magnification to image the fine-scale details of studied objects is a narrow DOF, so only a small portion of an obliquely imaged sample is sharp. This partially sharp image is referred to as “a narrow DOF image”. This poses a major challenge to photogrammetric reconstructions of small-scale morphological features, such as fracture wall roughness in shale rocks. This problem is circumvented by using the technique of focus stacking. The FS method consists of the following steps:

- (1) Collecting a set of images, systematically changing the camera-to-object distance while maintaining a stable focusing distance (Fig. 1).
- (2) Detecting the sharp sectors of each input image.
- (3) Combining the individual sharp parts of the input images into a single sharp image, referred to as the “extended DOF image”.

In the last step, it is crucial to rescale and transform the sharp sectors to restore the overall perspective of the output image. In this work, Helicon Focus software was used to perform an automated FS procedure. In Helicon Focus, the depth-map method (method B) of rendering with the following settings was chosen: radius – 50 and smoothness – 1. According to the software manual, this choice of method and parameters should yield the best results for images of a “simple surface with no sudden changes in surface level” (HeliconSoft, 2018). It was assumed that the rock-sample surfaces were relatively smooth, continuous and contained no large height gradients (such as hundreds of micrometres between neighbouring pixels). The radius parameter determines the size of the kernel used to calculate the contrast for pixels. Thus, larger kernels result in smoother edges of the sharpness mask (a mask for pixels in focus, understood as pixels with a large enough contrast), but the rendered image is also less vulnerable to the halo effect (HeliconSoft, 2018). Using a larger radius produces less jagged sharpness masks and allows for minimising the smoothness parameter, which controls the image softening used to smooth transitions between adjacent image portions.

First an estimate of the DOF is needed for the imaging set-up in order to choose a proper interval step for the rail system. The theoretical DOF can be approximated by:

$$DOF = \frac{2CE}{M^2} \quad (1)$$

where C is the maximum allowed circle of confusion, E denotes the effective aperture and M is the magnification. The effective aperture is a function of the magnification:

$$E = N(M + 1) \quad (2)$$

where N is the relative aperture, expressed as the f-number. The maximum allowed circle of confusion C in equation (1) can be set to a semi-arbitrary value, depending on what is accepted as sharp by the user (Savazzi, 2011). The C parameter can be treated as a sharpness criterion which determines how sharp image parts need to be within the expected DOF. A larger C results in a wider DOF, but less sharp image regions are classified as in DOF. For a specific camera and lens set-up, the upper limit of C is open-ended. However, even though the lower limit can be set as well, it cannot be smaller than the size of the Airy disc (Savazzi, 2011). Otherwise, the calculated DOF will be “hidden” under the blur introduced by diffraction. The size of the Airy disc D is controlled by the diffraction effect, which is a function of the effective aperture. It can be calculated for a specific wavelength of light λ as:

$$D = 2.43932\lambda E. \quad (3)$$

Since digital photography uses the visible spectrum of light, this work chose λ to be the mean visible wavelength of 580nm. Considering the sharpness to be as high as physically possible for the set-up, with reference to Savazzi (2011) parameter C was set to the size of the Airy disc, and the DOF was calculated using equation (1) (see Fig. 2). It is important to note that, for a constant lens aperture N , the Airy disc will increase with increasing magnification (Fig. 2). The relative aperture has the largest influence on the final DOF. The difference between the DOF for a relative aperture of f/8 and of f/5.6 reaches 30% (see Fig. 2). To find the optimal relative aperture for the Canon lens, a direct sharpness test was performed. For each full aperture stop, 10 photographs were taken of a test object

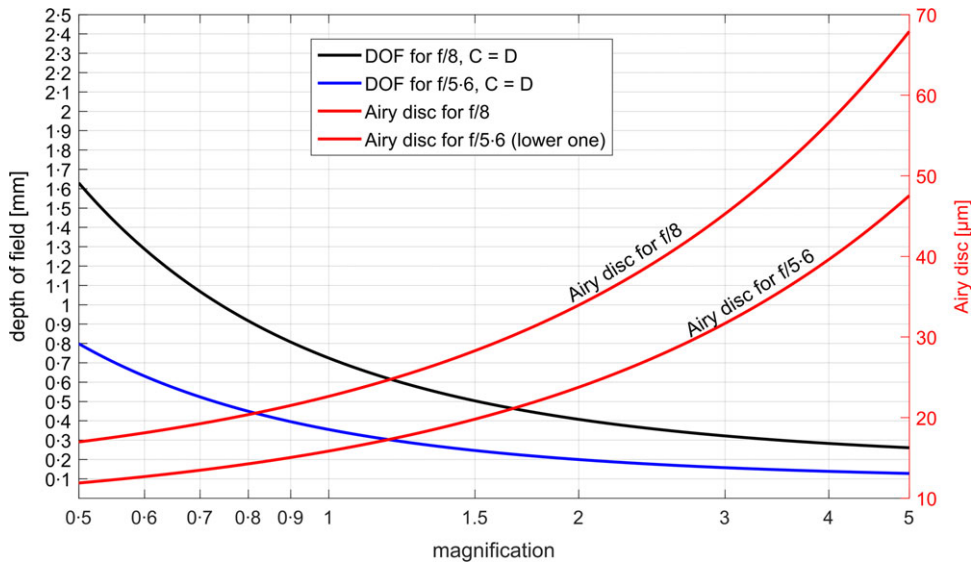


FIG. 2. Depth of field (left y axis) as a function of the magnification for two relative apertures of f/8 and f/5.6. The solid blue and black lines represent calculations for the maximum allowed circle of confusion (C) set equal to the Airy disc. The red lines give the size of the Airy disc (right y axis) as a function of magnification.

with a high colour-intensity gradient, keeping the camera parameters constant. Then the image part was chosen which was in focus in all photographs and the mean gradient was computed. The higher the image gradient, the sharper the edges are; thus, this method can indicate the relative sharpness of photographs. To compare such a sharpness measure for different relative apertures, it is essential to ensure that all images represent the same object or portion of an object, which always needs to be in focus. Analysing the results of the sharpness test (Fig. 3), a relative aperture of f/8 was chosen as a compromise between DOF reduced by a low relative aperture and blur introduced due to diffraction effects for high relative apertures. Following this, the DOF for the hardware was estimated as 0.7 mm (for a magnification of 1:1 with $C=D$ set to 0.0226 mm (about 5 GSD), and relative aperture equal to f/8 (Fig. 2)).

White-light Interferometry

To assess the accuracy of this FS-based photogrammetric analysis, the research directly compared a reconstructed low-amplitude (tens of micrometres) fracture roughness in a shale sample to high-accuracy measurements obtained using a white-light interferometer (WLI) (Hadizadeh et al., 2012; Renard et al., 2012; Faoro et al., 2016). The WLI measurements were performed using a Wyko NT1100 WLI on a damped table with Veeco software. For the comparison published here, the WLI measurements were taken with a $5\times$ Veeco objective and a field-of-view lens of 0.5, producing a total magnification of $2.5\times$. The manufacturer specifies that this results in a lateral (X and Y direction) resolution of $2\mu\text{m}/\text{pixel}$. The field of view of the set-up in this research resulted in maximum object measurements of $1280\mu\text{m} \times 960\mu\text{m}$. To measure larger areas, an in-built stitching function was implemented, with a 20% overlap between each image. The measurement for each

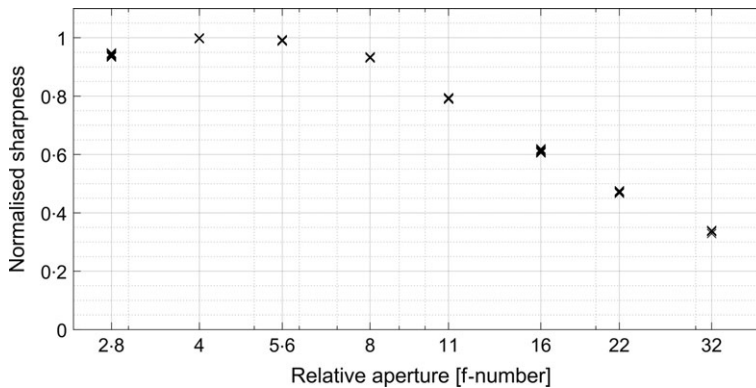


FIG. 3. Normalised image sharpness against relative aperture. The sharpness is given by mean image gradient.

sample was preceded by calibration of the vertical scanning imaging mode of the interferometer using a mirror with a $10\text{ }\mu\text{m}$ height step. Using the vertical scanning interferometry (VSI) mode, the theoretical vertical resolution of this Wyko NT1100 should be 3 nm . In practice, the vertical accuracy depends to some extent on the properties of the scanned object and specific hardware settings. The shale rock samples in this experiment exhibit poor and irregular reflectivity; furthermore, a local surface slope affects WLI accuracy (Xie et al., 2013). Note that, for some pixels, data quality is insufficient to accurately determine the height, which is either related to insufficient exposure (for example, due to shadows in larger pores) or to a large difference in reflectance with neighbouring pixels. This results in incomplete data coverage (holes) or a noisy signal, though never extending over more than 15% of the total imaged surface area. To eliminate outliers from the data and reduce the error, density filtering is used, where all points with fewer than 19 neighbours within an $8\text{ }\mu\text{m}$ radius were deleted. This leads to a maximum of 30% of holes randomly dispersed over the total surface, which still provides 15 million points per 1 cm^2 . Given the extremely high point density and high vertical resolution of the method, white-light interferometry data is used as a reference model which can be compared to the photogrammetric reconstruction of the real fractured shale sample to assess its quality.

Synthetic Models

For the synthetic experiments, four different types of reference roughness models were generated using the method of correlated random fields (Adler et al., 2013). In this approach, the rough surface is characterised by the summit–summit/valley–valley correlation lengths in the X and Y directions and the Hurst exponent, which governs the scaling properties of the roughness. An artificial square-bounded rough surface was generated (Fig. 4) with an edge length of 1.2 cm , a maximum height difference of $138.85\text{ }\mu\text{m}$, a signal standard deviation (s_{std}) of $19\text{ }\mu\text{m}$, and X and Y correlation lengths of 1.2 and 0.6 mm , respectively. The Hurst exponent was set to 0.75 , and 2400 points were used in each direction to discretise the signal. The mean absolute deviation Ra was $15.14\text{ }\mu\text{m}$. The distribution of the local surface height is Gaussian, hence the standard deviation of the height difference $std(\Delta Z)$ between the reference surface and an uncorrelated surface characterised by the same statistical properties can be expressed as $s_{std} \sqrt{2}$, which is

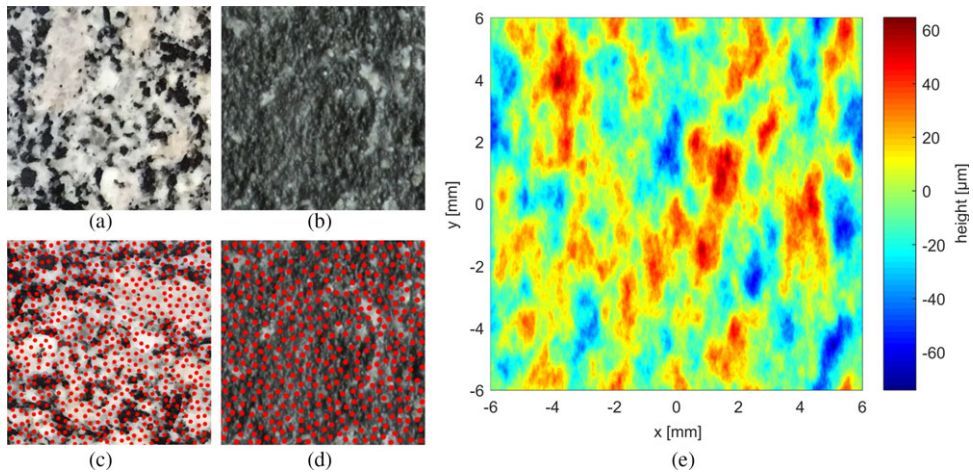


FIG. 4. The four types of texture and the synthetic surface. Textures are shown as a $4\text{ mm} \times 4\text{ mm}$ portion and are: (a) shale; (b) granite; (c) dotted shale; and (d) dotted granite. (e) Synthetic surface morphology. Parameters of the synthetic surface: X correlation length is 1.2 mm ; Y correlation length is 0.6 mm ; Hurst exponent is 0.75 ; and signal standard deviation (s_{std}) is $19\text{ }\mu\text{m}$.

$26.8\text{ }\mu\text{m}$. The X and Y correlation lengths were set to a 2:1 ratio to produce directional anisotropy and simulate structures, or parts of structures, like ripple marks or slickenside. Candela et al. (2012) report a Hurst exponent in natural rocks of between 0.5 and 0.9 , thus a value from this interval was chosen. Four different textures were wrapped onto the generated synthetic surface to create the four various types of reference roughness models. The first two types have base textures produced using representative photographs of natural granite and shale samples. To obtain the two remaining texture types, the action of a laser-based *random pattern projector* (Osela, 2018) was simulated by adding a random dot pattern consisting of 23 880 points (according to the device specification) on top of the granite and shale base textures. The radius of each dot and the minimum distance between the nearest dot boundaries was $20\text{ }\mu\text{m}$, while the mean distance between the dot boundaries was $26\text{ }\mu\text{m}$. This allowed a digital investigation into the use of a potential texture improvement by projecting extra patterns onto physical samples as proposed by Koutsoudis et al. (2015) to improve the texture of weakly textured objects. The positions of the dots were generated using the random sequential adsorption (RSA) algorithm (Feder, 1980) to ensure a certain degree of anti-clustering. The texturised models were named *shale*, *granite*, *dotted shale* and *dotted granite*, as shown in Figs. 4(a) to (d), respectively.

Misfit Measurements

Different reference models were used to study the impact of the various parameters on the accuracy of photogrammetric reconstructions. In the synthetic tests, the four synthetic models generated by the correlated random fields were used (Fig. 4). To validate the photogrammetric roughness measurements of the final sample, the scanned WLI section of shale was used as a reference model. In all cases, for a correct evaluation of the reconstruction errors, it was crucial to accurately align (translate, rotate and scale) the reconstructed point clouds with the reference models. This was a two-step process. Firstly,

the two point clouds were roughly aligned using CloudCompare software, based on the iterative closest point (ICP) algorithm (Besl and McKay, 1992; Chen and Medioni, 1992). Secondly, point clouds were finely aligned using the authors' own MATLAB code by minimising the standard deviation of the height difference ($std(\Delta Z)$) between the reference model and reconstructed surface. The code is based on the built-in optimisation function called *Fminsearch* and tries to find the lowest $std(\Delta Z)$ as a function of the rotation, translation and scaling of one of the input models. The point-to-point height difference is then measured to obtain a 2D error map of local height difference. The standard deviation of this local height difference provides a single value as a measure of global error. The local and global height differences are used as the prime error measures in this study.

In the case of reference models with textures (so only the synthetic tests), the use of SiftGPU allows the identification of the lateral misfit (similar to the distortion in photographs) by identifying the corresponding point pairs in the reference and reconstructed models via the following steps:

- (1) The textures of the aligned reconstructed and reference models are projected onto the same x - y plane.
- (2) The colour values in the irregularly distributed points of the model are interpolated to form a regularly sampled, top-view ortho-image for each of the two models.
- (3) The SiftGPU algorithm is used (the same procedure as used in the photogrammetric reconstruction) to find and match the location of keypoints. This allows the computation of the displacement vectors.
- (4) The mean in-plane rotation, translation and dilatation are removed from the reconstructed model.
- (5) The relative lateral misfit of the reconstructed point cloud is measured as mean lateral misfit, which is denoted by $mean(U)$.

Since the WLI only measures topography and does not provide information on the texture of the shale sample, the lateral error cannot be determined for the photogrammetric model relative to the WLI reference dataset.

The software used for the photogrammetric reconstruction uses a random sampling approach. Therefore, some reconstruction details are not necessarily exactly reproducible, leading to small differences for each software execution despite using fixed settings. The reference model was chosen to be the mean of 10 reconstructions, and the repeatability of reconstruction (RR) was measured by comparing those 10 reconstructions to the averaged reference model using $std(\Delta Z)$.

TESTS

To estimate the accuracy of the proposed photogrammetric analysis workflow for low-amplitude fracture roughness, three series of tests (two synthetic and one based on a real rock sample) were performed which allowed the isolation of the errors associated with the individual steps of the reconstruction. The first synthetic test showed the self-error of the software used, whereas the second synthetic test investigated the accuracy of FS and its influence on the accuracy of the final photogrammetric reconstruction. The third test applied the FS-enhanced photogrammetric method to a natural fracture surface found in a shale sample. This sample was from a borehole core, obtained from a depth of approximately

4 km in the Pomeranian region in Poland (for more details on the sample material, see Pluymakers et al. (2017)).

Photogrammetric Reconstruction Self-error

The first test aimed at assessing the self-error introduced by the VisualSFM photogrammetric procedure while reconstructing the fracture surface according to the reconstruction workflow described above. To this end, ideal (infinite DOF) images of a synthetic texturised rough surface were generated (Fig. 4) and its morphology reconstructed with a varying number of images and camera locations. The main goal was to estimate the influence of the number of input images (which directly determines the workload) and the type of surface texture on the reconstruction accuracy. For each synthetic fracture surface model (shale, granite, dotted shale and dotted granite), a set of images were prepared using the freely available software Blender (Blender, 2018). Blender allows the preparation of a scene with 3D objects and render images, simulating the action of a camera with prescribed properties. The camera and lens characteristics were set according to the parameters of the Canon 5DSR camera. Thus, the image sensor size, pixel count, focal length and magnification were set to 36 mm \times 24 mm, 8688 \times 5792 pixels (50.3 megapixels), 100 mm and 1:1, respectively. However, the test purposely used an infinite DOF and disabled geometric distortions. The camera location was contained within a sphere centred at the sample centre and the optical axis was chosen at an angle of either 45°, 60°, 75° or 90° with respect to the base plane of the rough surface. The azimuthal spacing between the generated images increased when increasing the inclination angle (Fig. 5). In total, 32 images were generated.

To check the influence of camera locations and surface texture, the point clouds of all four synthetic texturised models were reconstructed using the seven image subsets listed in Table I. The reconstructed models were translated, rotated and rescaled to allow for a direct comparison to the reference model. Fig. 6 depicts the standard deviation of the height difference $std(\Delta Z)$ between the reference model and reconstructed point clouds. Reconstructions generated from four or five images in subsets I, II and III lead to the lowest accuracy due to a weak angular coverage (image positioning) of the sample surface, and thus the highest accompanying $std(\Delta Z)$ ranges from 1.5 to 9.5 μm . Subsets I and II have the largest spread of $std(\Delta Z)$ among the four different texturised models (Fig. 6). For subsets IV to VII, with 10 to 32 input images, the measured $std(\Delta Z)$ are significantly lower, ranging from 0.8 to 2 μm (Fig. 6). Besides subset VII, the shale model generates the best results of the four different texture models. Enhancing the textures with dot patterns (dotted shale, dotted granite), which simulate the “random pattern projector”, yields no significant improvement. In subsets IV to VII, the differences between $std(\Delta Z)$ measured for natural rock textures (shale, granite) and their enhanced versions (dotted shale, dotted granite) reach about 0.5 μm .

To check the repeatability of the reconstructions, subset IV was selected with the shale texture (the same subset was later used to check the repeatability for other tests). The repeatability (RR) for this sample yielded 0.63 μm and is of the same order as the differences among the standard deviations $std(\Delta Z)$ measured for subsets IV to VII as well as the differences between the results generated for various textures used in these subsets.

As described in previous sections, there was a lateral error component in photogrammetric reconstructions, which was quantified with $mean(U)$. The same trends applied as with the vertical error: for all the textures, the surfaces reconstructed from subsets I to III are characterised by a relatively large lateral misfit with a high spread, with $mean(U)$

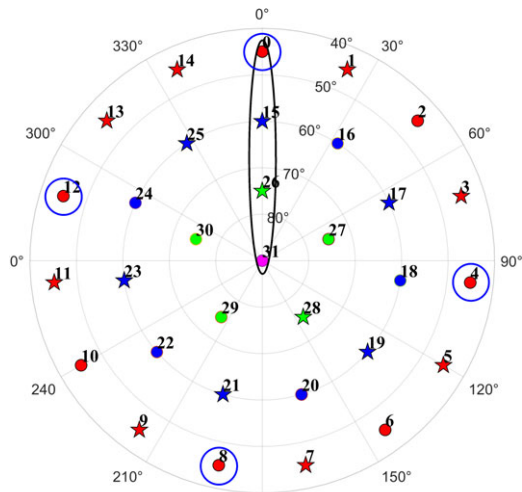


FIG. 5. Normals to the planes of the Blender images shown in the stereo plot. For the marker legend see Table I.

TABLE I. Image indices and orientation used to group images into subsets. See also Fig. 5.

Subset number	I	II	III	IV	V	VI	VII
Image index	0, 4, 8, 12	0, 15, 26, 31	26–30	15–25	0–14	See ss	0–31
Azimuth/ Dip	0/45 96/45 192/45 288/45	0/45 0/60 0/75 0/90	0/75 72/75 144/75 216/75 288/75	0/60 33/60 65/60 72/60 98/60 131/60 164/60 196/60 229/60 262/60 295/60 327/60	0/45 24/45 48/45 72/45 96/45 120/45 144/45 168/45 192/45 216/45 240/45 264/45 288/45 312/45 336/45	0/45 48/45 96/45 144/45 168/45 192/45 240/45 264/45 288/45 312/45 336/45 0/90	0/45; 24/45 48/45; 72/45 96/45; 120/45 144/45; 168/45 192/45; 216/45 240/45; 264/45 288/45; 312/45 336/45; 0/60; 33/60 65/60; 98/60 131/60; 164/60 196/60; 229/60 262/60; 295/60 312/60 327/60 0/75; 72/75 144/75; 216/75 288/75; 0/90

Marker on Fig. 5			Red	Blue	Green	Filled circle	All
------------------	---	---	-----	------	-------	---------------	-----

ss: 0, 2, 4, 6, 8, 10, 12, 16, 18, 20, 22, 24, 27, 29, 30, 31

up to 180 μm (Fig. 7). Even by eye, the resulting point clouds from subsets I and II are deformed, where the original square outline of the model is reconstructed as a trapezoid, rectangle or rhombus. However, the lateral error component for the reconstructions in subsets IV to VII falls in narrow intervals with $\text{mean}(U)$ in the range between 1.25 and 1.9 μm . For all models in subset V, the so-called dome error was observed (Wackrow and Chandler, 2008), which can be related to improperly detected and removed optical distortion. Note that for every reconstruction, regardless of the texture used or image subset, the largest misfit occurs in the corners. In the subsets with low misfits (subsets IV to VII), the model texture has no significant impact on the lateral error $\text{mean}(U)$.

Focus Stacking Distortion

In this second synthetic test, the quality of the output images produced by the FS procedure was examined using the following steps:

- (1) Using the Blender software, a flat surface texturised with the shale texture was generated.
- (2) A single infinite DOF image was rendered, which served as a reference image, together with a set of narrow DOF images for this surface. To render the narrow DOF images, an $f/8$ relative aperture was simulated, with a stepwise change in the camera-to-object distance.
- (3) Assuming a 40% overlap between the regions in focus, with the DOF estimated to be 0.72 mm, 1:1 magnification and a 60° angle between the camera's optical axis and the surface, 32 input images were needed to produce one extended DOF image.
- (4) After generation of the extended DOF image in the Helicon Focus software, the lateral misfit was measured between the infinite and extended DOF images.

During the rendering of the narrow DOF images, the distance from the camera to the scene centre changes for every shot. However, the distance from the camera to the part of the surface in the DOF is constant; thus, the sharp segments of each input photograph have a similar GSD (ground pixel size). Note that, for a fixed camera position, in the perspective view presented by the camera lens, the segments that are located further away from the camera should have a larger GSD, whereas the segments closer to the camera should have a smaller GSD. The FS software is capable of rescaling (downscaling or upscaling) the segments to avoid any non-consistent transitions between the neighbouring segments (Fig. 8) and ensure the restoration of the perspective view.

Theoretically, the application of uniform shrinking or stretching to an image should not affect the photogrammetric reconstruction that follows, since it produces exactly the same result as a change of focal length or the camera-to-object distance. Unfortunately, the reconstruction of the perspective view during FS is not perfect and it may also introduce shear-like distortions (Fig. 8(c)). The authors have named this residual, non-dilation distortion *stacking distortion*. Stacking distortion remains present in the final output image and thus it affects its quality and thereby the quality of the photogrammetric reconstruction. For the case presented in Fig. 8, the mean lateral misfit $\text{mean}(U)$ of the extended DOF image is equal to 1.34 pixel, which corresponds to 5.3 μm for a 4.13 μm GSD and the 1:1 magnification. The stacking distortion observed in Fig. 8 can be split into two components. The first component is a barrel distortion which can be, at least partially, removed in the VisualSFM software. The second one is present as local distorted strips, 100 to 200 pixels

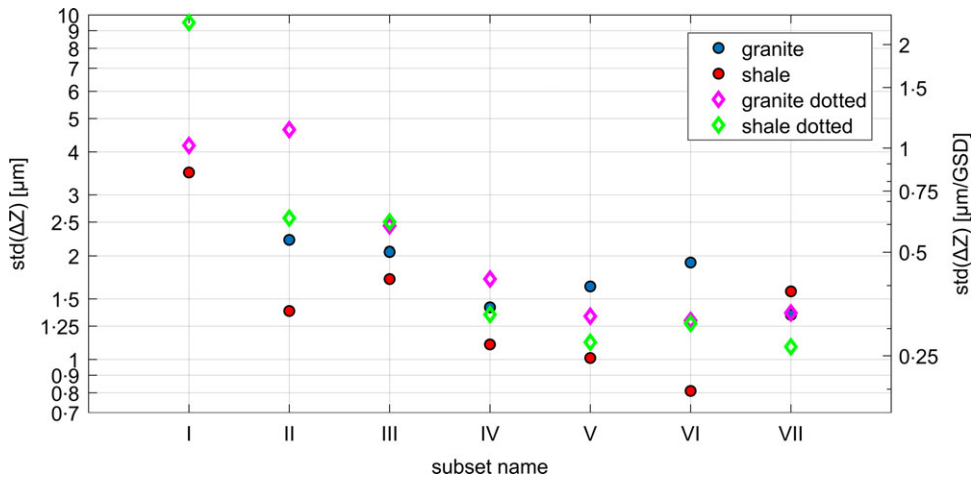


FIG. 6. Standard deviation of height difference $std(\Delta Z)$ between synthetic and reconstructed models. A low $std(\Delta Z)$ is an indication of high quality. The reconstruction for the granite pattern in subset I failed.

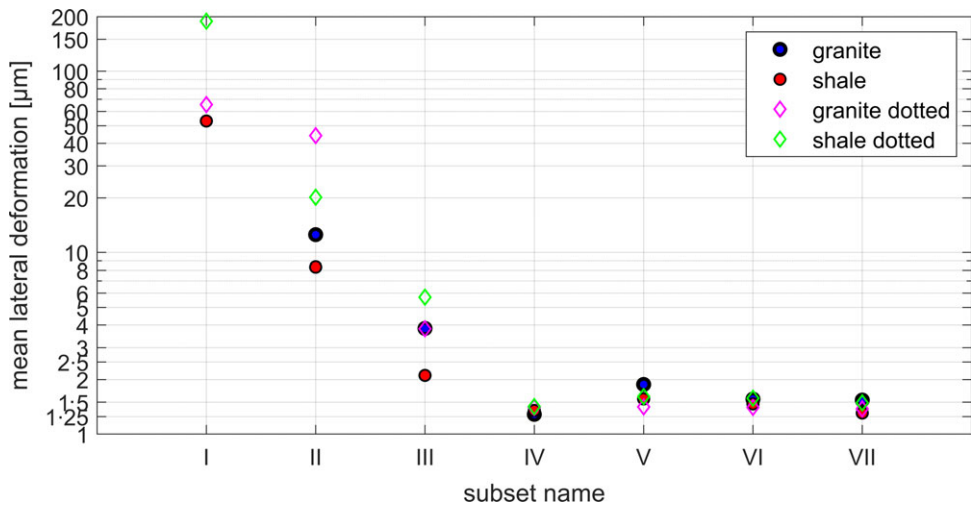


FIG. 7. Mean lateral misfit $mean(U)$. A low $mean(U)$ is an indication of high quality. The reconstruction for the granite pattern in subset I failed.

wide, related to inexact positioning and rescaling of the sharp parts of narrow DOF images. The second component can strongly affect the final 3D reconstruction.

The aim of the second part of this experiment was to determine the influence of the FS technique, used to obtain the extended DOF images, on the accuracy of the resulting photogrammetric reconstruction. To this end, the Blender software was first used to generate sets of images of a synthetic rough surface wrapped with the shale texture. To generate these images, the Canon 5DSR camera was simulated with a typical, finite DOF, and use of the same set of camera locations as in the first experiment (Fig. 5). However, for each of the 32

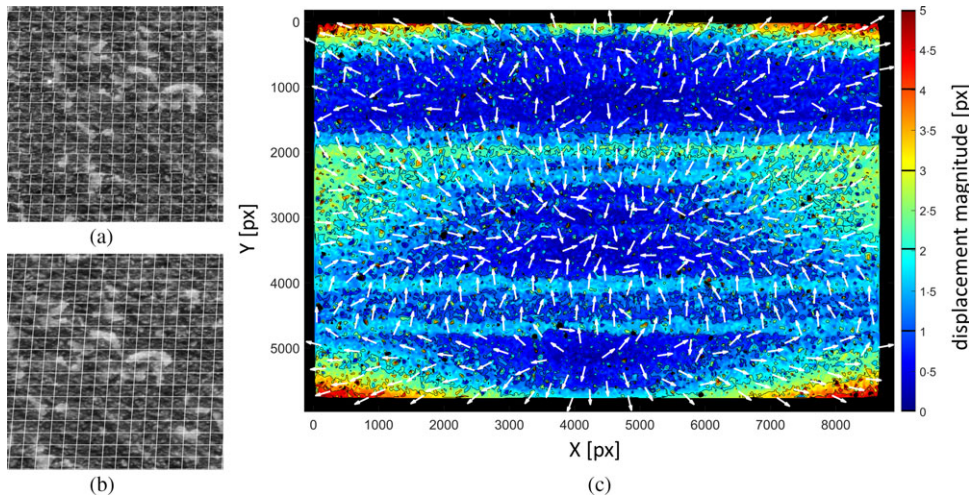


FIG. 8. Distortion due to focus stacking. A flat surface with a shale texture enhanced by a square grid. Images (a) with and (b) without segment rescaling, shown for a 1000×1000 pixel region. The angle between the camera's optical axis and the surface is 60° . (c) Final distortion field (stacking distortion) after removing the overall dilation.

camera positions, the virtual camera was moved in a stepwise fashion along its optical axis such that the entire surface was covered with partially sharp, narrow DOF images. Basically, this simulates the role of the macro rail in the hardware set-up (Fig. 1). From equation (1), the DOF was 0.72 mm for the simulated relative aperture of $f/8$ and the targeted magnification of 1:1. Assuming an approximate 40% overlap between the sharp sectors, the distance between the adjacent narrow DOF images was set as 0.45 mm. Three series of narrow DOF images were generated for a magnification of 1:1 with the following settings:

- FS1: a relative aperture set to $f/4$, to show the effects of improperly calculated DOF or insufficient overlap between sharp regions.
- FS2: a relative aperture of $f/8$.
- FS3: a relative aperture of $f/8$ and a textured flat background around the rough synthetic surface.

For each series, 704 narrow DOF images were created, which were then used to generate 32 extended DOF images for each series. In series FS1 and FS2, artefacts were present close to the edges and, in particular, the corners of the extended DOF images. For further reconstructions, these marginal regions were manually removed from the extended DOF images generated for these two series. Next, 3D models for all the camera position subsets were reconstructed (Fig. 5). In this phase of the experiment, all reconstruction attempts for the sparse subsets I and II failed. It was observed that using too narrow a DOF during the FS reconstruction phase leads to a high final error. Introducing a textured background in the FS3 series eliminated edge artefacts in the extended DOF images and improved the quality of the final stacked image. This resulted in more accurate surface reconstructions in comparison to the FS2 series with no background pattern.

The mean lateral misfit observed for the FS3 series is two to three times larger when the extended DOF images are used instead of the synthetic infinite DOF ones (Fig. 9). For all the reconstructions in the FS3 series, a strip-like distortion pattern was observed, which is probably related to non-exact matching between the sharp regions in the input images during the FS procedure. The elevated level of the lateral misfit is also partly related to the dome effect (Wackrow and Chandler, 2008), which is visible in the lateral misfit fields obtained. On the other hand, the vertical error ($std(\Delta Z)$) observed for the FS3 series is similar to the error observed in the first synthetic tests (Figs. 8 and 9). Checking the repeatability RR of the photogrammetric processing for subset IV and the FS3 series, results in $RR=0.82\mu\text{m}$, for 10 reconstructions, thus of the same order as the standard deviation $std(\Delta Z)$ of the synthetic tests. The tests show that using a sufficient overlap between the narrow DOF images and adding an auxiliary texturised background are crucial steps for FS-enhanced photogrammetric reconstructions.

Photogrammetry Compared with White-light Interferometry

To validate the FS-enhanced photogrammetric reconstruction of the roughness of the fractured shale, a comparison of its results with the high-resolution WLI measurements of the same fracture surface was performed. Following the technical specifications of the WLI, the WLI measurement error should be negligible compared to the photogrammetric error. Thus, the difference between the WLI and the photogrammetric data was treated as the error of the photogrammetric method. For photogrammetric reconstruction, to obtain the necessary series of narrow DOF images, the Canon 5DS R camera was used with the 100 mm macro lens and the macro rail. Considering the results of the synthetic tests, it was decided to use the camera positioning as in subset IV with the following settings: (a) 30 partially sharp images to reconstruct one extended DOF image; (b) sum of extended DOF images – 15; (c) a camera-to-surface angle of about 60° ; (d) a relative aperture of $f/8$; (e) an exposure time of 0.8 s; (f) an ISO of 100; and (g) a white balance of 6500 K lamp colour temperature. According to Reznicek et al. (2016), a typical RAW to JPEG conversion does not result in a noticeable decrease in reconstruction accuracy. The output images were taken as JPEGs generated directly by the camera with the JPEG quality set to fine.

The WLI scan and the photogrammetric reconstruction of the shale surface are shown in Figs. 10(a) and (b), and with the corresponding histograms in Figs. 10(d) and (e). The global roughness parameters R_a and RMS are 11.8 and $14.8\mu\text{m}$ for WLI, while those obtained from photogrammetric data are 11.1 and $14.0\mu\text{m}$. Note that the lack of textural data for the WLI scans renders it impossible to detect any lateral misfit between the two measurements. The error level was therefore evaluated by aligning the two point clouds using the height difference between WLI and photogrammetry as an error indicator. For approximately 1 cm^2 scan area, the standard deviation of the height difference $std(\Delta Z)$ was equal to $6.5\mu\text{m}$ (Fig. 10). The repeatability (RR) of the reconstruction was $3.8\mu\text{m}$ based on 10 samples. The height difference appeared as random noise with a Gaussian distribution, except for some sparse outliers; it exhibits no significant correlation to the surface height and shows no dome effects (Figs. 10(c) and (f)).

To further characterise the error structure, a power spectrum density (PSD) analysis was performed (Candela et al., 2012; Mahboob Kanafi et al., 2015). The PSD curves of both surfaces exhibit a similar slope and hence similar scaling properties for wavelengths above $20\mu\text{m}$ (Fig. 11). The misfit for shorter wavelengths can be related to the different point density of the WLI and photogrammetric data. The photogrammetric data density depends on the effective cell size for which PMVS2/CMVS tries to reconstruct at least one patch.

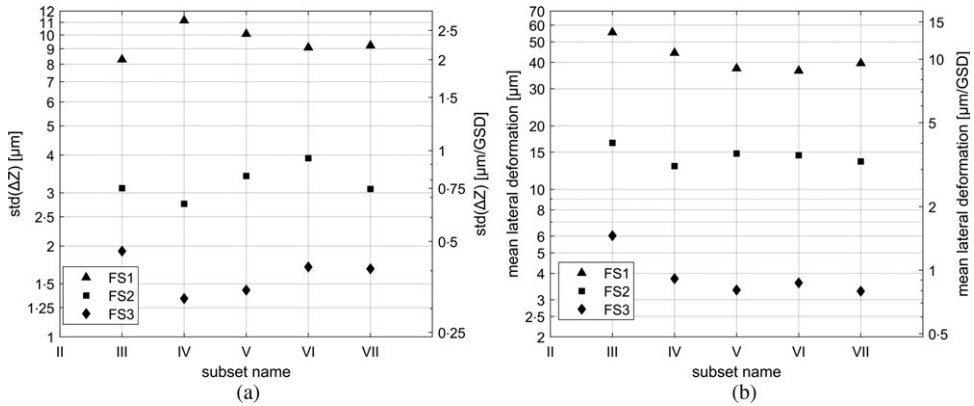


FIG. 9. (a) Standard deviation of height differences between synthetic and reconstructed models. (b) Mean lateral deformation.

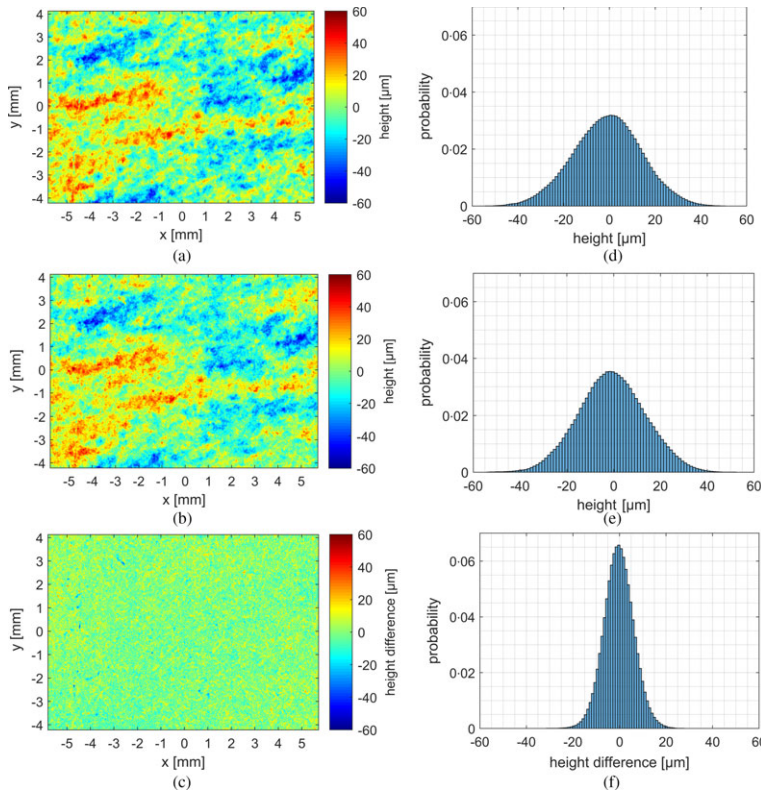


FIG. 10. Comparison of WLI and photogrammetric measurements. (a) WLI scan; (b) photogrammetric scan; (c) height difference map; (d) height histogram from WLI scan; (e) height histogram from photogrammetric scan; (f) height difference histogram.

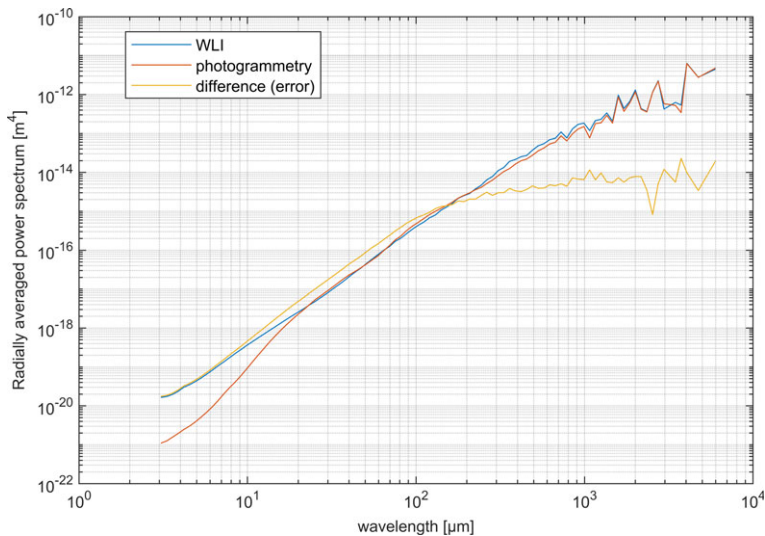


FIG. 11. Power spectrum density (PSD) of the WLI scan, photogrammetric reconstruction and signal height difference (error).

The default parameter for the cell size is four times GSD, which gave a cell size of $16.5\text{ }\mu\text{m}$ in the experiments. For wavelengths below about $150\text{ }\mu\text{m}$, the error spectrum showed a similar scaling as the WLI and photogrammetry data, albeit with an even greater amplitude, implying a misfit between the two datasets. The error component for wavelengths exceeding $150\text{ }\mu\text{m}$ exhibited a much weaker slope and amplitude than the data spectrums, indicating that the two reconstructions were a good fit in this range. Furthermore, high- and low-pass filtering were used to split both the WLI and photogrammetric data signals into short- and long-wavelength components, with a threshold wavelength equal to $150\text{ }\mu\text{m}$. The correlation coefficient of the long-wavelength components was 0.96, which confirms that they are little affected by the measurement errors. In contrast, the correlation coefficient calculated for the short-wavelength components was 0.15, which indicates that these parts of the reconstructions were highly affected by the errors. The RMS of the short-wavelength components was approximately $3.2\text{ }\mu\text{m}$ with amplitudes reaching up to $10\text{ }\mu\text{m}$. On the other hand, the standard deviation of the height difference between the short-wavelength components of the WLI and photogrammetric data was $4.2\text{ }\mu\text{m}$ (Fig. 11) – if the signals under comparison were totally uncorrelated, the standard deviation would reach $4.5\text{ }\mu\text{m}$.

DISCUSSION

Instead of providing theoretical consideration of the maximum available accuracy, the authors treated the results of the first synthetic test, where the input images were free of distortion and blur introduced by narrow DOF, as the maximum accuracy that can be obtained by the given set-up. Effects of this test showed both $std(\Delta Z)$ and $mean(U)$ to be below $2\text{ }\mu\text{m}$ (0.5 GSD), which suggested this to be the accuracy limit dependent on the software algorithm. The second synthetic test performed with enabled DOF and FS also results in $std(\Delta Z)$ being below $2\text{ }\mu\text{m}$, but with a two-times greater $mean(U)$ of below $4\text{ }\mu\text{m}$. From this it can be seen that applying the FS technique results mostly in lateral

deformation. In the third test the authors have estimated the error level ($std(\Delta Z)$) of the FS-enhanced photogrammetric reconstruction of natural shale fracture roughness at $6.5\ \mu\text{m}$, which suggested that introducing a real, imperfect camera is a major factor that reduced the accuracy. Given that the shale surface had a low-amplitude roughness, with an RMS of $14.8\ \mu\text{m}$ and an amplitude reaching $100\ \mu\text{m}$, this error is on the high side. This implies that the photogrammetric reconstruction can only be used to accurately describe and quantify morphological features with amplitudes larger than $10\ \mu\text{m}$. The size of the morphological features of the surface is correlated with the conditions during crack formation, as well as the rock type and rock constituents. In shales, the fracture roughness may reach amplitudes up to a few hundreds of micrometres (Zhou et al., 2016) or more, especially if some remains of mineralisation occurred on fracture surfaces. In coarser grained rock types, such as granites or sandstones, the roughness amplitude in hand specimens can reach up to several millimetres (Ponson et al., 2007; Candela et al., 2012; Singh et al., 2016; Vogler et al., 2017). With regard to intergranular cracking, coarser grained rocks may produce higher amplitudes of surface features and be better suited for photogrammetric reconstructions than shales. On the other hand, some features, such as plumose structures, are better developed in fine-grained rocks. Even so, the authors advise caution, since the method in this paper produces significant errors for amplitudes less than $10\ \mu\text{m}$ and a wavelength below $150\ \mu\text{m}$. Since such errors on small-length scales may add to the error for any characterisation on a large scale, it is advised that users of FS-enhanced photogrammetric reconstruction should filter off the small-scale, short-wavelength features prior to further signal analysis – especially when working with small amplitude or/and small length scales of roughness features.

In these tests, a systematic increase in the reconstruction accuracy with increasing quality of the input was observed by choosing: (1) a sufficient number of camera positions; (2) a good overlap between narrow DOF images; and (3) using a background texture. In the synthetic tests with simulated images, the accuracy was high, although some tailored image processing was required during the stacking of narrow DOF input images. The tests performed with real images showed a lower accuracy level, which can be partly related to various optical aberrations (especially lens distortion), the noise of the camera sensor and general imperfections of the imaging system. It was observed that surface reconstructions based on five or fewer images exhibited a significantly higher error level than the average. On the other hand, no further accuracy improvement was observed for models with 10 or more input images (Figs. 7 and 8). Thus, 6 to 10 extended DOF images are optimal considering the presented approach and surface character. For relatively flat surfaces, such as the shale tested here, changing camera inclination angles does not affect the reconstruction accuracy. It is recommended to use camera-to-surface angles near 60° , which should provide good specimen coverage by images and reduce the number of narrow DOF images required to create the extended DOF image.

To perform accurate photogrammetric reconstructions of small objects, such as the roughness of a fine-grained rock-like shale, valid input images with a wide DOF are needed. In this FS-enhanced photogrammetric method, extended DOF images generated by the FS procedure were used. The reported tests have shown that FS constitutes a critical stage of the proposed measurement routine, and image processing related to the FS technique can potentially be a source of reconstruction errors. However, using a sufficient overlap between sharp regions of the narrow DOF input images and an auxiliary background, where the entire camera frame is filled with a textured object, significantly reduces the level of reconstruction errors. As sharpness detection in FS software is based on

contrast (gradient) detection, it is suggested that a contrasting pattern composed of small features is used as a background texture.

Koutsoudis et al. (2015) suggested improving textureless objects by projecting artificial patterns. However, the synthetic tests in this research have shown that natural textural features of rocks such as granite and shale exhibit a sufficiently rich pattern to ensure the detection of keypoints, feature matching and camera positioning for further dense point-cloud reconstruction. Texture enhancements by projecting a random monochrome dot pattern have proven not to be beneficial in this work. The authors speculate that projecting simple dot patterns for objects with insufficient textural features, or projecting more complicated patterns on natural fracture surfaces, may still be beneficial.

Since this work focused on the effects related to FS and textural enhancement, it has deliberately used the default software parameters in VisualSFM. However, taking advantage of the usage of high-resolution input images (50 megapixels) required changing the maximum number of detected keypoints and the maximum working dimension for feature detection. According to the VisualSFM software manual, there are 56 parameters in total that control the reconstruction: 22 parameters for SiftGPU, 22 parameters for MBA and 12 parameters for PMVS2/CMVS. Changing any of the default parameters may have an effect on the reconstruction stability, density and accuracy, together with required computation time. Thus, some accuracy improvement could still potentially be achieved by changing the software settings for any given application.

CONCLUSIONS

This research performed a set of tests to assess the accuracy of a SfM photogrammetric method, enhanced by FS, to measure shale rock fracture roughness. The use of both synthetic and physical object tests allowed the indication of the major sources of reconstruction error and to determine the level of reconstruction accuracy. The main conclusions are:

- (1) The error in photogrammetric reconstruction is highly correlated with the quality of the input images. High-quality equipment and appropriate environmental conditions are thus essential to increase the accuracy of the reconstruction.
- (2) Reconstructions based on images captured using 6 to 10 camera locations at an inclination angle of about 60° seem to be optimal with regard to the workload and final accuracy.
- (3) Natural textures of rocks such as granite and shale are rich enough for photogrammetric purposes. Using textural enhancements, such as random dot patterns, produces no significant improvement in the reconstruction quality.
- (4) Photogrammetric imaging combined with FS can be used to reconstruct rock fracture surfaces with a roughness amplitude down to tens of micrometres. The FS-enhanced photogrammetric method is a good compromise between cost, final reconstruction accuracy and the relatively large area of a scanned surface.

ACKNOWLEDGEMENTS

The research has been performed in the framework of the ShaleMech project (“An integrated geomechanical investigation to enhance gas extraction from the Pomeranian shale formations”) funded by BlueGas – Polish Shale Gas Programme by the National Centre for

Research and Development (Grant No. BG2/ShaleMech/14) and the ShaleSeq project (“Physicochemical effects of CO₂ sequestration in the Pomeranian gas bearing shales”) funded/co-funded from Norway Grants in the Polish–Norwegian Research Programme operated by the National Centre for Research and Development (Grant No. POL-NOR/234198/100/2014). Anne Plumakers is currently supported by the Dutch Foundation for Scientific Research (NWO) (No. 016.Veni.181.036).

REFERENCES

- ADLER, P. M., THOVERT, J.-F. and MOURZENKO, V. V., 2013. *Fractured Porous Media*. Oxford University Press, Oxford, UK. 175 pages.
- ALEKSANDROWSKI, P., 1985. Graphical determination of principal stress directions for slickenside lineation populations: an attempt to modify Arthaud’s method. *Journal of Structural Geology*, 7(1): 73–82.
- AMELI, P., ELKHOURY, J. E. and DETWILER, R. L., 2013. High-resolution fracture aperture mapping using optical profilometry. *Water Resources Research*, 49(10): 7126–7132.
- ANGELIER, J., 1984. Tectonic analysis of fault slip data sets. *Journal of Geophysical Research: Solid Earth*, 89(B7): 5835–5848.
- BABADAGLI, T., REN, X. and DEVELI, K., 2015. Effects of fractal surface roughness and lithology on single and multiphase flow in a single fracture: an experimental investigation. *International Journal of Multiphase Flow*, 68: 40–58.
- BAHAT, D., 1987. Correlation between fracture surface morphology and orientation of cross-fold joints in Eocene chalks around Beer Sheva, Israel. *Tectonophysics*, 136(3): 323–333.
- BAHAT, D., 1991. *Tectonofractography*. Springer, Berlin, Germany. 354 pages.
- BARTON, N., 1973. Review of a new shear-strength criterion for rock joints. *Engineering Geology*, 7(4): 287–332.
- BARTON, N. and CHOUHEY, V., 1977. The shear strength of rock joints in theory and practice. *Rock Mechanics*, 10(1): 1–54.
- BESL, P. J. and MCKAY, N. D., 1992. A method for registration of 3-D shapes. *IEEE Transactions on Pattern Analysis and Machine Intelligence*, 14(2): 239–256.
- BIANCONI, F., CATALUCCI, S., FILIPPUCI, M., MARSILI, R., MORETTI, M., ROSSI, G. and SPERANZINI, E., 2017. Comparison between two non-contact techniques for art digitalization. *Journal of Physics: Conference Series*, 882(1): 012005.
- BISTACCHI, A., GRIFFITH, W. A., SMITH, S. A. F., DI TORO, G., JONES, R. and NIELSEN, S., 2011. Fault roughness at seismogenic depths from LIDAR and photogrammetric analysis. *Pure and Applied Geophysics*, 168(12): 2345–2363.
- BLENDER, 2018. <https://www.blender.org/> [Accessed: 4th September 2018].
- BRODSKY, E. E., GILCHRIST, J. J., SAGY, A. and COLLETTINI, C., 2011. Faults smooth gradually as a function of slip. *Earth and Planetary Science Letters*, 302(1–2): 185–193.
- BROWN, S. R., 1995. Simple mathematical model of a rough fracture. *Journal of Geophysical Research: Solid Earth*, 100(B4): 5941–5952.
- BRUSH, D. J. and THOMSON, N. R., 2003. Fluid flow in synthetic rough-walled fractures: Navier–Stokes, Stokes, and local cubic law simulations. *Water Resources Research*, 39(4): 1085. article 5. 15 pages.
- CANDELA, T., RENARD, F., KLINGER, Y., MAIR, K., SCHMITTBUHL, J. and BRODSKY, E. E., 2012. Roughness of fault surfaces over nine decades of length scales. *Journal of Geophysical Research: Solid Earth*, 117(B8): article B08409. 30 pages.
- CANON, 2017. *Canon EOS 5DS and 5DSR*. <https://www.usa.canon.com/internet/portal/us/home/explore/product-showcases/cameras-and-lenses/high-resolution-eos-5ds-vs-5dsr/> [Accessed: 19th February 2018].
- CHEN, Y. and MEDIONI, G., 1992. Object modelling by registration of multiple range images. *Image and Vision Computing*, 10(3): 145–155.
- COOK, N. G. W., 1992. Natural joints in rock: mechanical, hydraulic and seismic behaviour and properties under normal stress. *International Journal of Rock Mechanics and Mining Sciences & Geomechanics Abstracts*, 29(3): 198–223.
- CORRADETTI, A., MCCAFFREY, K., DE PAOLA, N. and TAVANI, S., 2017a. Evaluating roughness scaling properties of natural active fault surfaces by means of multi-view photogrammetry. *Tectonophysics*, 717: 599–606.

- CORRADETTI, A., TAVANI, S., RUSSO, M., ARBUÉS, P. C. and GRANADO, P., 2017b. Quantitative analysis of folds by means of orthorectified photogrammetric 3D models: a case study from Mt. Catria, Northern Apennines, Italy. *Photogrammetric Record*, 32(160): 480–496.
- DEGRAFF, J. M. and AYDIN, A., 1987. Surface morphology of columnar joints and its significance to mechanics and direction of joint growth. *GSA Bulletin*, 99(5): 605–617.
- FAORO, I., ELSWORTH, D. and CANDELA, T., 2016. Evolution of the transport properties of fractures subject to thermally and mechanically activated mineral alteration and redistribution. *Geofluids*, 16(3): 396–407.
- FEDER, J., 1980. Random sequential adsorption. *Journal of Theoretical Biology*, 87(2): 237–254.
- FICKER, T., 2017. Fractal properties of joint roughness coefficients. *International Journal of Rock Mechanics and Mining Sciences*, 94: 27–31.
- FICKER, T. and MARTIŠEK, D., 2012. Digital fracture surfaces and their roughness analysis: applications to cement-based materials. *Cement and Concrete Research*, 42(6): 827–833.
- FUJII, Y., TAKAHASHI, M. and HORI, S., 2007. Three-dimensional topography of fracture surfaces obtained by a digital photogrammetric technique. *International Journal of the Japanese Committee for Rock Mechanics*, 3(1): 31–36.
- FURUKAWA, Y. and PONCE, J., 2010. Accurate, dense, and robust multiview stereopsis. *IEEE Transactions on Pattern Analysis and Machine Intelligence*, 32(8): 1362–1376.
- GADELMAWLA, E. S., KOURA, M. M., MAKSOUD, T. M. A., ELEWA, I. M. and SOLIMAN, H. H., 2002. Roughness parameters. *Journal of Materials Processing Technology*, 123(1): 133–145.
- GALLAND, O., BERTENSEN, H. S., GULDSTRAND, F., GIROD, L., JOHANNESSEN, R. F., BJUGGER, F., BURCHARDT, S. and MAIR, K., 2016. Application of open-source photogrammetric software MicMac for monitoring surface deformation in laboratory models. *Journal of Geophysical Research: Solid Earth*, 121(4): 2852–2872.
- GALLANT, J. C., MOORE, I. D., HUTCHINSON, M. F. and GESSLER, P., 1994. Estimating fractal dimension of profiles: a comparison of methods. *Mathematical Geology*, 26(4): 455–481.
- GRANSHAW, S. I., 2016. Photogrammetric terminology: third edition. *Photogrammetric Record*, 31(154): 210–251.
- HADIZADEH, J., MITTEMPERGHER, S., GRATIER, J.-P., RENARD, F., DI TORO, G., RICHARD, J. and BABAIE, H. A., 2012. A microstructural study of fault rocks from the SAFOD: implications for the deformation mechanisms and strength of the creeping segment of the San Andreas Fault. *Journal of Structural Geology*, 42: 246–260.
- HANEBERG, W. C., 2007. Directional roughness profiles from three-dimensional photogrammetric or laser scanner point clouds. *1st Canada–U.S. Rock Mechanics Symposium*, Vancouver, Canada. 7 pages.
- HELICONSOFT, 2018. *Understanding the Focus Stacking Parameters*. <https://www.heliconsoft.com/helicon-focus-main-parameters/> [Accessed: 29th August 2018].
- HENG, B. C. P., CHANDLER, J. H. and ARMSTRONG, A., 2010. Applying close range digital photogrammetry in soil erosion studies. *Photogrammetric Record*, 25(131): 240–265.
- KOUTSOUDIS, A., IOANNAKIS, G., VIDMAR, B., ARNAUTOGLU, F. and CHAMZAS, C., 2015. Using noise function-based patterns to enhance photogrammetric 3D reconstruction performance of featureless surfaces. *Journal of Cultural Heritage*, 16(5): 664–670.
- LANARO, F., 2000. A random field model for surface roughness and aperture of rock fractures. *International Journal of Rock Mechanics and Mining Sciences*, 37(8): 1195–1210.
- LATO, M. J. and VÖGE, M., 2012. Automated mapping of rock discontinuities in 3D lidar and photogrammetry models. *International Journal of Rock Mechanics and Mining Sciences*, 54: 150–158.
- LEE, H.-S. and AHN, K.-W., 2004. A prototype of digital photogrammetric algorithm for estimating roughness of rock surface. *Geosciences Journal*, 8(3): 333–341.
- LI, Y. and HUANG, R., 2015. Relationship between joint roughness coefficient and fractal dimension of rock fracture surfaces. *International Journal of Rock Mechanics and Mining Sciences*, 75: 15–22.
- LOCKLEY, M. G., MCCREA, R. T., BUCKLEY, L. G., LIM, J. D., MATTHEWS, N. A., BREITHAUP, B. H., HOUCK, K. J., GIERLINSKI, G. D., SURMIK, D., KIM, K. S., XING, L., KONG, D. Y., CART, K., MARTIN, J. and HADDEN, G., 2016. Theropod courtship: large scale physical evidence of display arenas and avian-like scrape ceremony behaviour by Cretaceous dinosaurs. *Nature Scientific Reports*, 6: article 18952. 10 pages.
- MAHBOOB KANAFI, M., KUOSMANEN, A., PELLINEN, T. K. and TUONONEN, A. J., 2015. Macro- and micro-texture evolution of road pavements and correlation with friction. *International Journal of Pavement Engineering*, 16(2): 168–179.
- MANDELBROT, B. B., 1983. *The Fractal Geometry of Nature*. W. H. Freeman, New York, USA. 468 pages.

- MARTÍNEZ, S., CUESTA, E., BARREIRO, J. and ÁLVAREZ, B., 2010. Methodology for comparison of laser digitizing versus contact systems in dimensional control. *Optics and Lasers in Engineering*, 48(12): 1238–1246.
- MORELLI, G. L., 2014. On joint roughness: measurements and use in rock mass characterization. *Geotechnical and Geological Engineering*, 32(2): 345–362.
- MOURZENKO, V. V., THOVERT, J.-F. and ADLER, P. M., 2001. Permeability of self-affine fractures. *Transport in Porous Media*, 45(1): 89–103.
- NIEMINSKI, N. M. and GRAHAM, S. A., 2017. Modeling stratigraphic architecture using small unmanned aerial vehicles and photogrammetry: examples from the Miocene East Coast Basin, New Zealand. *Journal of Sedimentary Research*, 87(2): 126–132.
- NILSSON, M., EDELBRO, C. and SHARROCK, G., 2012. Small scale joint surface roughness evaluation using digital photogrammetry. *Eurock 2012: ISRM International Symposium on Rock Engineering and Technology for Sustainable Underground Construction*, Stockholm, Sweden. 13 pages.
- ODLING, N. E., 1994. Natural fracture profiles, fractal dimension and joint roughness coefficients. *Rock Mechanics and Rock Engineering*, 27(3): 135–153.
- OSELA, 2018. *Structured Light and Laser Beam Shaping Solutions*. <https://www.osela.com/products/random-pattern-projector/> [Accessed: 3rd September 2018].
- PETIT, J. P., 1987. Criteria for the sense of movement on fault surfaces in brittle rocks. *Journal of Structural Geology*, 9(5–6): 597–608.
- PLUYMAKERS, A., KOBCHENKO, M. and RENARD, F., 2017. How microfracture roughness can be used to distinguish between exhumed cracks and in-situ flow paths in shales. *Journal of Structural Geology*, 94: 87–97.
- PONSON, L., AURADOU, H., PESSEL, M., LAZARUS, V. and HULIN, J.-P., 2007. Failure mechanisms and surface roughness statistics of fractured Fontainebleau sandstone. *Physical Review E*, 76(3 Part 2): article 036108.
- POON, C. Y. and BHUSHAN, B., 1995. Comparison of surface roughness measurements by stylus profiler, AFM and non-contact optical profiler. *Wear*, 190(1): 76–88.
- POON, C. Y., SAYLES, R. S. and JONES, T. A., 1992. Surface measurement and fractal characterization of naturally fractured rocks. *Journal of Physics D: Applied Physics*, 25(8): 1269–1276.
- RAJA, J., MURALIKRISHNAN, B. and FU, S., 2002. Recent advances in separation of roughness, waviness and form. *Precision Engineering*, 26(2): 222–235.
- RENARD, F., MAIR, K. and GUNDERSEN, O., 2012. Surface roughness evolution on experimentally simulated faults. *Journal of Structural Geology*, 45: 101–112.
- REZNICEK, J., LUHMANN, T. and JEPPIING, C., 2016. Influence of raw image preprocessing and other selected processes on accuracy of close-range photogrammetric systems according to VDI 2634. *International Archives of Photogrammetry, Remote Sensing and Spatial Information Sciences*, 41(B5): 107–113.
- SAVAZZI, E., 2011. *Digital Photography for Science: Close-up Photography, Macro photography and Photomacrography*. Lulu Enterprises, Raleigh, North Carolina, USA. 704 pages.
- SCHMITTBUHL, J., STEYER, A., JOUNIAUX, L. and TOUSSAINT, R., 2008. Fracture morphology and viscous transport. *International Journal of Rock Mechanics and Mining Sciences*, 45(3): 422–430.
- SCHÖNING, J. and HEIDEMANN, G., 2015. Evaluation of multi-view 3D reconstruction software. *Lecture Notes in Computer Science*, 9257: 450–461.
- SINGH, K. K., SINGH, D. N. and GAMAGE, R. P., 2016. Effect of sample size on the fluid flow through a single fractured granitoid. *Journal of Rock Mechanics and Geotechnical Engineering*, 8(3): 329–340.
- TATONE, B. S. A. and GRASSELLI, G., 2012. Quantitative measurements of fracture aperture and directional roughness from rock cores. *Rock Mechanics and Rock Engineering*, 45(4): 619–629.
- TERPSTRA, T., VOITEL, T. and HASHEMIAN, A., 2016. A survey of multi-view photogrammetry software for documenting vehicle crush. *SAE Technical Paper*, 2016-01-1475. 31 pages.
- THOM, C. A., BRODSKY, E. E., CARPICK, R. W., PHARR, G. M., OLIVER, W. C. and GOLDSBY, D. L., 2017. Nanoscale roughness of natural fault surfaces controlled by scale-dependent yield strength. *Geophysical Research Letters*, 44(18): 9299–9307.
- TSANG, Y. W. and WITHERSPOON, P. A., 1981. Hydromechanical behavior of a deformable rock fracture subject to normal stress. *Journal of Geophysical Research: Solid Earth*, 86(B10): 9287–9298.
- TWISS, R. J. and MOORES, E. M., 2007. *Structural Geology*. Second edition. Freeman, New York, USA. 736 pages.
- VOGLER, D., WALSH, S. D. C., BAYER, P. and AMANN, F., 2017. Comparison of surface properties in natural and artificially generated fractures in a crystalline rock. *Rock Mechanics and Rock Engineering*, 50(11): 2891–2909.

- VOLLGGER, S. A. and CRUDEN, A. R., 2016. Mapping folds and fractures in basement and cover rocks using UAV photogrammetry, Cape Liptrap and Cape Paterson, Victoria, Australia. *Journal of Structural Geology*, 85: 168–187.
- WACKROW, R. and CHANDLER, J. H., 2008. A convergent image configuration for DEM extraction that minimises the systematic effects caused by an inaccurate lens model. *Photogrammetric Record*, 23(121): 6–18.
- WALSH, J. B., 1981. Effect of pore pressure and confining pressure on fracture permeability. *International Journal of Rock Mechanics and Mining Sciences & Geomechanics Abstracts*, 18(5): 429–435.
- WANG, L., CARDENAS, M. B., SLOTTKE, D. T., KETCHAM, R. A. and SHARP, J. M., JR., 2015. Modification of the Local Cubic Law of fracture flow for weak inertia, tortuosity, and roughness. *Water Resources Research*, 51(4): 2064–2080.
- WENZEL, K., ROTHERMEL, M., FRITSCH, D. and HAALA, N., 2013. Image acquisition and model selection for multi-view stereo. *International Archives of Photogrammetry, Remote Sensing and Spatial Information Sciences*, 40(5/W1): 251–258.
- WICKENS, E. H. and BARTON, N. R., 1971. The application of photogrammetry to the stability of excavated rock slopes. *Photogrammetric Record*, 7(37): 46–54.
- WU, C., 2007. *SiftGPU: a GPU Implementation of Scale Invariant Feature Transform (SIFT)*. <http://cs.unc.edu/~ccwu/siftgpu> [Accessed: 23rd February 2017].
- WU, C., 2013. Towards linear-time incremental structure from motion. *International Conference on 3D Vision*, Seattle, Washington, USA. Pages 127–134.
- WU, C., AGARWAL, S., CURLESS, B. and SEITZ, S. M., 2011. Multicore bundle adjustment. *IEEE Conference on Computer Vision and Pattern Recognition*, Colorado Springs, Colorado, USA. Pages 3057–3064.
- XIE, H., WANG, J.-A. and KWAŚNIEWSKI, M. A., 1999. Multifractal characterization of rock fracture surfaces. *International Journal of Rock Mechanics and Mining Sciences*, 36(1): 19–27.
- XIE, J., LIU, X. R., WU, K. K., LU, Y. J. and LI, P., 2013. Evaluation on 3D micro-ground profile accuracy of micro-pyramid-structured Si surface using an adaptive-orientation WLI measurement. *Precision Engineering*, 37(4): 918–923.
- YONG, R., YE, J., LI, B. and DU, S.-G., 2018. Determining the maximum sampling interval in rock joint roughness measurements using Fourier series. *International Journal of Rock Mechanics and Mining Sciences*, 101: 78–88.
- ZHANG, G. C., KARAKUS, M., TANG, H. M., GE, Y. F. and JIANG, Q. Q., 2017. Estimation of joint roughness coefficient from three-dimensional discontinuity surface. *Rock Mechanics and Rock Engineering*, 50(9): 2535–2546.
- ZHOU, T., ZHANG, S. C., FENG, Y., SHUAI, Y. Y., ZOU, Y. S. and LI, N., 2016. Experimental study of permeability characteristics for the cemented natural fractures of the shale gas formation. *Journal of Natural Gas Science and Engineering*, 29: 345–354.
- ZIMMERMAN, R. W. and BODVARSSON, G. S., 1996. Hydraulic conductivity of rock fractures. *Transport in Porous Media*, 23(1): 1–30.
- ZOU, L., JING, L. and CVETKOVIC, V., 2015. Roughness decomposition and nonlinear fluid flow in a single rock fracture. *International Journal of Rock Mechanics and Mining Sciences*, 75: 102–118.

Résumé

Dans les applications en champ proche, la capacité de la photogrammétrie optique à reconstruire avec précision la rugosité à l'échelle submillimétrique n'est pas évidente. Cet article présente une étude des mesures de rugosité des fractures rocheuses à une échelle fine avec une évaluation soignée de l'erreur. La méthode combine les techniques de structure par le mouvement et d'empilement de mises au point, en utilisant un équipement grand public et un logiciel gratuit ou bon marché. L'approche est testée en premier lieu avec des données synthétiques pour vérifier l'influence du nombre et de la position des caméras, de la texture de l'objet et du traitement de l'image, par empilement de mises au point. La méthode optimisée est ensuite utilisée pour mesurer la surface d'une fracture naturelle de schiste. Pour estimer la précision, les résultats ont été comparés à un jeu de données de référence de haute précision obtenu par interférométrie en lumière blanche. L'écart-type de l'erreur de la méthode est de 6,5 µm et est lié aux structures morphologiques dont la longueur d'onde est inférieure à 150 µm et l'amplitude inférieure à 10 µm.

Zusammenfassung

In geologischen Nahbereichsanwendungen der Photogrammetrie ist es offen, ob die Oberflächenrauheit mit einer Genauigkeit von unter einem Millimeter rekonstruiert werden kann. Diese Studie analysiert Rauheitsmessungen mit Photogrammetrie. Es werden die Techniken von Structure-from-Motion mit einer Schärfentieferweiterung (Fokus-stapelung) kombiniert und dabei herkömmliche Kameras und freie oder kostengünstige Software verwendet. Der Ansatz wird zunächst an synthetischen Daten getestet, um die Einflüsse von Anzahl und Standorten der Aufnahmen, der Objekttextur und der Bildverarbeitung mit Fokus-Stapelung festzustellen. Der daraus resultierende optimierte Arbeitsfluss wird für Messungen einer Bruchoberfläche eines natürlichen Schiefergesteins eingesetzt. Zur Abschätzung der Genauigkeit werden die Ergebnisse mit einem hochgenauen Referenzdatensatz aus Weißlichtinterferometrie verglichen. Die Standardabweichung der vorgeschlagenen Methode liegt bei $6.5\ \mu\text{m}$, und ist bezogen auf morphologische Strukturen mit Wellenlängen unter $150\ \mu\text{m}$ und Amplituden kleiner als $10\ \mu\text{m}$.

Resumen

En aplicaciones de fotogrametría de objeto cercano, no está claro si es posible reconstruir con precisión la rugosidad del objeto a escala submilimétrica. Este artículo presenta un estudio de las mediciones de rugosidad de fractura de roca a escala fina con una evaluación cuidadosa del error. El flujo de trabajo combina las técnicas de estructura de movimiento y apilamiento de enfoque, utilizando equipos de consumo y software gratuito o asequible. El método se prueba primero con datos sintéticos para verificar la influencia del número y la posición de las cámaras, la textura del objeto y el proceso de la imagen mediante el apilamiento de enfoque. En segundo lugar, el flujo de trabajo optimizado se utiliza para medir una superficie natural de fractura de roca de esquisto. Para estimar la precisión, los resultados se compararon con un conjunto de datos de referencia de alta precisión obtenido por interferometría de luz blanca. La desviación estándar del error en el método es de $6.5\ \mu\text{m}$, y está relacionada con estructuras morfológicas con longitudes de onda inferiores a $150\ \mu\text{m}$ y amplitudes menores de $10\ \mu\text{m}$.

摘要

在近距离应用中, 尚不清楚光学摄影测量是否能够精确地重建亚毫米级粗糙度。本文介绍了对细小岩石破裂粗糙度测量的研究, 并仔细评估了其误差。其工作流程结合了运动恢复结构和焦点合成技术, 使用消费级设备以及免费或价廉的软件。本方法首先使用仿真数据测试, 通过焦点合成来研究相机的树木与位置、对象纹理和图像处理方法对结果的影响。然后, 以前述研究分析优化后的工作流程测量天然页岩岩石破裂面。为了估计准确度, 以白光干涉测量法的高精度成果作为比对参考。本方法的误差标准偏差为 $6.5\ \mu\text{m}$, 对应于波长小于 $150\ \mu\text{m}$, 振幅小于 $10\ \mu\text{m}$ 的形态结构。